Special Issue

Deep Neural Network for Scleral Spur Detection in Anterior Segment OCT Images: The Chinese American Eye Study

Benjamin Y. Xu[1], Michael Chiang[2], Anmol A. Pardeshi[1], Sasan Moghimi[3], and Rohit Varma[4]

[1] Roski Eye Institute, Department of Ophthalmology, Keck School of Medicine at the University of Southern California, Los Angeles, CA, USA
[2] Sol Price School of Public Policy, University of Southern California, Los Angeles, CA, USA
[3] Hamilton Glaucoma Center, Shiley Eye Institute, Department of Ophthalmology, University of California, San Diego, La Jolla, CA, USA
[4] Southern California Eye Institute, CHA Hollywood Presbyterian Medical Center, Los Angeles, CA, USA

Purpose: To develop a deep neural network that detects the scleral spur in anterior segment optical coherence tomography (AS-OCT) images.

Methods: Participants in the Chinese American Eye Study, a population-based study in Los Angeles, California, underwent complete ocular examinations, including AS-OCT imaging with the Tomey CASIA SS-1000. One human expert grader provided reference labels of scleral spur locations in all images. A convolutional neural network (CNN)-based on the ResNet-18 architecture was developed to detect the scleral spur in each image. Performance of the CNN model was assessed by calculating prediction errors, defined as the difference between the Cartesian coordinates of reference and CNN-predicted scleral spur locations. Prediction errors were compared with intragrader variability in detecting scleral spur locations by the reference grader.

Results: The CNN was developed using a training dataset of 17,704 images and tested using an independent dataset of 921 images. The mean absolute prediction errors of the CNN model were 49.27 ± 42.07 μm for X-coordinates and 47.73 ± 39.70 μm for Y-coordinates. The mean absolute intragrader variability was 52.31 ± 47.75 μm for X-coordinates and 45.88 ± 45.06 μm for Y-coordinates. Distributions of prediction errors for the CNN and intragrader variability for the reference grader were similar for X-coordinates ($P = 0.609$) and Y-coordinates ($P = 0.378$). The mean absolute prediction error of the CNN was 73.08 ± 52.06 μm and the mean absolute intragrader variability was 73.92 ± 60.72 μm.

Conclusions: A deep neural network can detect the scleral spur on AS-OCT images with performance similar to that of a human expert grader.

Translational Relevance: Deep learning methods that automate scleral spur detection can facilitate qualitative and quantitative assessments of AS-OCT images.

Introduction

Closure of the anterior chamber angle (ACA) is the primary risk factor for developing primary angle closure glaucoma (PACG), a leading cause of permanent vision loss worldwide.[1] Angle closure occurs when there is appositional or synechial contact between the trabecular meshwork (TM) and iris. Angle closure leads to impaired aqueous humor outflow and elevated intraocular pressure, an important risk factor for glaucomatous optic neuropathy.[2] Therefore, early detection of angle closure is crucial to prevent permanent vision loss, especially because there are effective treatments to alleviate angle closure.[3–5]

Gonioscopy is the current clinical standard for evaluating the ACA and detecting angle closure. However, gonioscopic assessments are subjective, qualitative, and limited by interexaminer variability.[6]

Anterior segment optical coherence tomography (AS-OCT) is an in vivo imaging method that provides an alternative to gonioscopy for evaluating the anterior segment and its structures, including the ACA.[7–9] AS-OCT images provide qualitative assessments of the ACA and quantitative measurements of ocular biometric parameters, some of which are risk factors for angle closure disease.[10–13] AS-OCT measurements also have excellent intradevice, intragrader, and intergrader reproducibility.[6,14–18] However, a long-standing limitation of AS-OCT is that image analysis is only semiautomated; a trained grader must manually identify specific anatomic structures before angle closure can be detected and quantified.[19–21] This time-intensive and expertise-dependent process has significantly hindered the clinical and research utility of AS-OCT.

The scleral spur is the key anatomic structure for assessing the ACA and detecting angle closure in AS-OCT images. The TM is poorly detectable by standalone AS-OCT devices, such as the Zeiss Visante (Carl Zeiss Meditec, Dublin, CA), Tomey CASIA SS-1000 (Tomey Corporation, Nagoya, Japan), and Heidelberg Anterion (Heidelberg Engineering, Heidelberg, Germany), owing to the wavelength of their scanning lasers. However, it is relatively easy to detect the scleral spur, which demarcates the posterior boundary of the TM.[22] Angle closure in AS-OCT images is defined by iridotrabecular contact (ITC), which is contact between the inner corneal curvature and iris anterior to the scleral spur.[15] In addition, quantitative measurements of angle width, lens position, to other biometric parameters are only accessible once the scleral spur has been detected.

Deep learning is a form of artificial intelligence that has proven to be an effective method for automating the analysis of ocular images, including AS-OCT images.[23–26] In this study, we combine deep learning methods and population-based AS-OCT data to develop and test a fully automated convolutional neural network (CNN) model for detecting the scleral spur in AS-OCT images.

Methods

Participants were recruited as part of the Chinese American Eye Study (CHES), a population-based, cross-sectional study that included 4572 Chinese participants aged 50 years and older residing in Monterey Park, California. As participants in CHES, patients received a complete eye examination by a trained ophthalmologist, including gonioscopy and AS-OCT imaging. Ethics committee approval was previously obtained from the University of Southern California Medical Center Institutional Review Board. All study procedures adhered to the recommendations of the Declaration of Helsinki. All study participants provided informed consent.

Inclusion criteria for the study included CHES participants who received AS-OCT imaging. Exclusion criteria included a history of media opacities that precluded visualization of intraocular structures. Participants with history of prior laser peripheral iridotomy, eye surgery (e.g., cataract extraction, incisional glaucoma surgery), or penetrating eye injury were not excluded. Both eyes from a single participant could be recruited so long as they fulfilled the inclusion and exclusion criteria.

Clinical Assessment

Gonioscopy was performed in the seated position with a Posner-type 4-mirror lens (Model ODPSG; Ocular Instruments, Inc., Bellevue, WA) under dark ambient lighting (0.1 cd/m^2) by two trained ophthalmologists (D.W., C.L.G.) masked to other examination findings. A 1-mm light beam was reduced to a narrow slit. Care was taken to avoid light from falling on the pupil and to avoid inadvertent indentation. The gonioscopy lens could be tilted to gain a view of the angle over the convexity of the iris. Angle closure was defined as any eye in which the pigmented TM could not be visualized in three or more angle quadrants.

AS-OCT imaging in CHES was performed in the seated position under dark ambient lighting (0.1 cd/m^2) before pupillary dilation by a single trained ophthalmologist (D.W.) with the Tomey CASIA SS-1000 swept-source Fourier-domain device (Tomey Corporation). There were 128 two-dimensional cross-sectional AS-OCT images acquired per eye. During imaging, the eyelids were gently retracted, taking care to avoid inadvertent pressure on the globe.

Image Processing and Analysis

Raw image data were imported into the SS-OCT Viewer software (version 3.0, Tomey Corporation). One human expert grader (grader 1, A.A.P.) masked to the identities and examination results of the participants, marked the scleral spurs in four images per eye; these labels of scleral spur locations were considered the reference standard. Before the current study, grader 1 underwent extensive training in scleral spur detection, including manual analysis of approximately 500 AS-OCT images (not included in the study) while supervised by at least one of two glaucoma special-
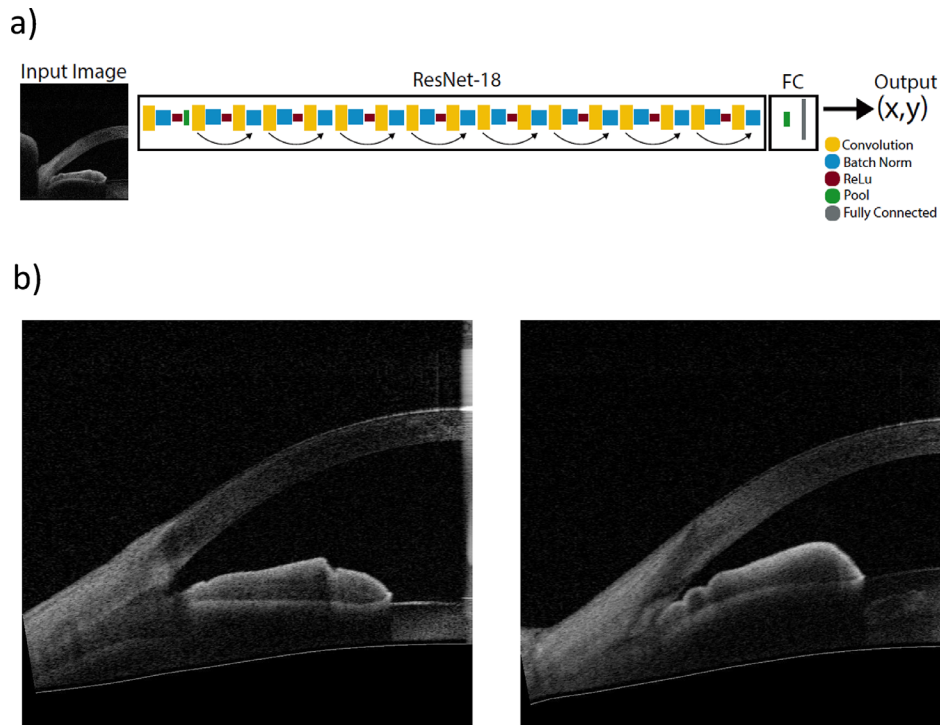
a)

b)

Figure 1. (a) Flow diagram of the ResNet-18 CNN architecture used to develop the model. Unmarked AS-OCT images were used as inputs to the CNN. The model predicted the Cartesian coordinates (X- and Y-locations) of the scleral spur. (b) Representative AS-OCT images used in CNN development. FC = fully connected; ReLu = rectified linear units.

ists (B.Y.X or R.V.). Four images were analyzed and exported in JPEG format per eye: the first image was oriented along the horizontal (temporal–nasal) meridian, and additional OCT images were evenly spaced 45° apart. Owing to a limitation in the SS-OCT Viewer software, scleral spur locations could only be exported when at least six of eight possible scleral spurs were marked. Thus, corrupt images and images with significant artifacts, including by the eyelids or arcus senilis, that precluded manual detection of the scleral spur by grader 1 were excluded. This step helped to minimize noise during CNN model training and testing. Images were divided in two along the vertical midline, and right-sided images were rotated about the vertical axis to standardize images with the ACA to the left and corneal apex to the right. No adjustments were made to image brightness or contrast. Image manipulations were performed in MATLAB (Mathworks, Natick, MA).

Before model training, images from 95% of participants were segregated into a training dataset. Images from the remaining 5% of participants were segregated into an independent test dataset. To prevent data leakage (e.g., intereye and intraeye correlations) between training and test datasets, multiple images acquired from a single participant appeared together in either the training or test dataset and were not split across both datasets. Data manipulations were performed in the Python programming language.

The reference grader (grader 1) and a second glaucoma fellowship-trained human grader (grader 2, B.Y.X.), both masked to participant identities, examination results, and original scleral spur locations, independently marked the scleral spur in all test dataset images. These locations were used to calculate metrics of intragrader and intergrader variability. Images reinspected as part of the test dataset could be further excluded owing to noise and artifacts that precluded attempts to mark the scleral spur by one or both of the graders.

Deep Learning Model Development

A deep CNN model was developed to predict the Cartesian coordinates of the scleral spur in individual AS-OCT images (Fig. 1). The original AS-OCT images had a standardized resolution of 900 (height) by 831 (width) pixels. Reference labels of scleral spur coordinates were based on manual analysis of these images by grader 1. The uppermost 69 pixels of each image, which did not contain any information about ocular structures, were cropped to make images

compatible with the ResNet architecture, which only accepts square images as inputs. These images (831 × 831 pixels) were automatically resized to 224 × 224 pixels by the ResNet architecture to be consistent with its original training dataset. Grayscale input images were preprocessed by normalizing RGB channels to have a mean of [0.485, 0.456, 0.406] and a standard deviation of [0.229, 0.224, 0.225]. Reference scleral spur coordinates were transposed and downsampled before training to match the new pixel coordinate space.

The deep learning model was a modified ResNet-18 CNN pretrained on the ImageNet Challenge dataset.[27] The final pooling and fully connected layers were removed and replaced by with a fully connected layer with two output nodes corresponding to X- and Y-coordinates. The Adam optimization algorithm and L1 loss was used to train the network. Transfer learning was first applied to train the final layer of the CNN.[28] Then all layers of the CNN were fine-tuned using backpropagation. Optimization was performed using L1 loss and the Adam optimization algorithm; L1 loss was used instead of L2 to reduce the effect of outliers in the training data. Scleral spur coordinates predicted by the CNN were then upsampled and transposed to match the pixel coordinate space of the original AS-OCT images. Pixels were then rescaled to micrometers (μm) based on the manufacturer-provided conversion rate of 1 pixel = 8 μm (width) × 10 μm (height).

Deep Learning Model Testing

The performance of the CNN model was assessed by calculating the error associated with the predicted Cartesian coordinates of each scleral spur location. X- and Y-coordinate prediction errors were calculated in micrometers by subtracting CNN-predicted coordinates from the corresponding reference coordinates 1. Intraobserver variability of X- and Y-coordinates were calculated in μm by subtracting the second set of scleral spur coordinates by grader 1 from corresponding reference coordinates. Intergrader variability of X- and Y-coordinates were calculated in micrometers by subtracting scleral spur coordinates by grader 2 from corresponding reference coordinates. Absolute error was calculated as: $\sqrt{(\text{X-coordinate error}^2 + \text{Y-coordinate error}^2)}$.

Histograms were plotted to visualize the distribution of X-coordinate, Y-coordinate, and absolute errors in 10 μm increments. The normality of error distributions was assessed with the Kolmogorov-Smirnov test. The Wilcoxon signed-rank test was used to compare three pairs of error distributions:

reference – CNN, reference – grader 1 (new), and reference – grader 2.

The CNN was retrained on different-sized random subsets of the training dataset to evaluate the effect of dataset size on algorithm performance. The size of the random subsets was increased in 2% to 10% increments.

Post Hoc Analysis of Sample Size

Based on our final sample size (921 images in the test dataset) and the largest standard deviation of errors associated with detecting X- and Y-coordinates of scleral spur location (78.24 μm for intergrader variability of X-coordinates), our study was powered to detect a difference of 7.5 μm with an alpha of 0.05 and a beta of 0.2. To put this number into context, 7.5 μm is smaller than both the width (8.0 μm) and height (10.0 μm) of a single pixel in the original AS-OCT images.

Results

Of the 4582 participants, 2210 (48.2%) enrolled in CHES underwent AS-OCT imaging. There were 114 participants (5.2%) who were excluded based on the exclusion criteria, with the majority ($N = 106$) being due to either corrupt or missing images or imaging artifacts. The complete study dataset included 18,664 AS-OCT images from 2333 eyes of 2096 participants. The mean and standard deviation of participant age was 60.2 ± 7.67 years (range, 50–94 years). There were 732 (34.9%) male participants and 1364 (65.1%) female. There were 4256 images (22.8%) that came from angle closure eyes and 14,408 (77.2%) that came from open angle eyes.

The CNN model was developed using a training dataset of 17,696 images from 2213 eyes of 1991 participants (95% of total participants) and corresponding scleral spur coordinates. The performance of the CNN model was assessed using a test dataset of 960 images from 120 eyes of 105 participants (5% of total participants). Of the 960 images, 39 (4.1%) were excluded owing to noise or artifacts that precluded attempts to mark the scleral spur by one or both of the graders. There was no overlap of participants between the training and test datasets. There were 223 images (24.2%) that came from angle closure eyes and 698 images (75.8%) that came from open angle eyes.

Table. Metrics of CNN Model Performance and Intragrader and Intergrader Variability in Open Angle, Angle Closure, and All Eyes (N = 921)

	CNN Prediction Error (µm)	Intragrader Variability (µm)	Intergrader Variability (µm)
All eyes (N = 921)			
X-coordinate	1.23 ± 64.80	0.82 ± 70.84	−43.56 ± 78.24
Y-coordinate	−0.56 ± 62.10	8.07 ± 63.53	−37.85 ± 73.49
Absolute X-coordinate	49.27 ± 42.07	52.31 ± 47.75	67.10 ± 59.27
Absolute Y-coordinate	47.73 ± 39.70	45.88 ± 45.06	63.59 ± 52.79
Absolute overall	73.08 ± 52.06	73.92 ± 60.72	97.34 ± 73.29
Open angle eyes (N = 698)			
X-coordinate	−1.06 ± 61.58	0.84 ± 67.95	−44.29 ± 77.54
Y-coordinate	−4.36 ± 57.11	3.19 ± 56.09	−43.06 ± 66.07
Absolute overall	69.22 ± 47.70	67.37 ± 56.82	96.10 ± 70.37
Angle closure eyes (N = 223)			
X-coordinate	8.41 ± 73.65	0.78 ± 79.39	−41.27 ± 80.53
Y-coordinate	11.37 ± 74.54 µm	31.60 ± 73.65	−21.52 ± 91.22
Absolute overall	85.16 ± 62.41	94.44 ± 67.70	101.21 ± 81.81

Deep Learning Model Performance

The mean prediction error of the CNN model was 1.23 ± 64.80 µm for X-coordinates and –0.56 ± 62.10 µ for Y-coordinates (Table, Fig. 2). The mean absolute prediction error of the CNN model was 49.27 ± 42.07 µm for X-coordinates, 47.73 ± 39.70 µm for Y-coordinates, and 73.08 ± 52.06 µm overall (Table). The mean intragrader variability of scleral spur location was 0.82 ± 70.84 µm for X-coordinates and 8.07 ± 63.53 µm for Y-coordinates (Table, Fig. 2). The mean absolute intragrader variability of scleral spur location was 52.31 ± 47.75 µm for X-coordinates, 45.88 ± 45.06 µm for Y-coordinates, and 73.93 ± 60.72 µm overall (Table). The mean intergrader variability of scleral spur location was –43.56 ± 78.24 µm for X-coordinates and −37.85 ± 73.49 µm for Y-coordinates (Table, Supplementary Fig. S1). The mean absolute intergrader variability of scleral spur location was 67.10 ± 59.27 µm for X-coordinates, 63.59 ± 52.79 µm for Y-coordinates, and 97.34 ± 73.29 µm for absolute values (Table).

The mean prediction errors tended to be lower for open angle compared with angle closure eyes (Table). The mean prediction errors of the CNN model were –1.06 ± 61.58 µm (open) and 8.41 ± 73.65 µm (closed) for X-coordinates, –4.36 ± 57.11 µm (open) and 11.37 ± 74.54 µm (closed) for Y-coordinates, and 69.22 ± 47.70 µm (open) and 85.16 ± 62.41 µm (closed) for absolute values. The mean intragrader variability of scleral spur location was 0.84 ± 67.95 µm (open) and 0.78 ± 79.39 µm (closed) for X-coordinates, 3.19 ± 56.09 µm (open) and 31.60 ± 73.65 µm (closed) for Y-coordinates, and 67.37 ± 56.82 µm (open) and 94.44 ± 67.70 µm (closed) µm for absolute values. The mean intergrader variability of scleral spur location was –44.29 ± 77.54 µm (open) and –41.27 ± 80.53 µm (closed) for X–coordinates, −43.06 ± 66.07 µm (open), and –21.52 ± 91.22 µm (closed) for Y-coordinates, and 96.10 ± 70.37 µm (open) and 101.21 ± 81.81 µm (closed) µm for absolute values.

The distribution of absolute prediction errors by the CNN was 40.61% within 50 µm, 76.22% within 100 µm, 90.88% within 150 µm, and 97.18% within 200 µm (Figs. 3 and 4). The distribution of errors from intragrader variability was 43.43% within 50 µm, 76.33% within 100 µm, 89.47% within 150 µm, and 95.22% within 200 µm. The distribution of errors from intergrader variability was 27.14% within 50 µm, 62.21% within 100 µm, 81.76% within 150 µm, and 91.64% within 200 µm.

One previous study used 80 µm along both the X- and Y-axes as a cutoff for clinically significant variability in detecting scleral spur locations.[14] In our study, 80.76% of predicted coordinates by the CNN model and 79.57% of repeat coordinates by grader 1 were within 80 µm of the reference coordinates along both the X- and Y-axes. 71.91% of coordinates by grader 2 were within 80 µm of the reference coordinates along both the X- and Y-axes.

The distributions of X- and Y-coordinate errors were not normally distributed (Kolmogorov-Smirnov test, $P < 0.001$) for any of the three comparisons:
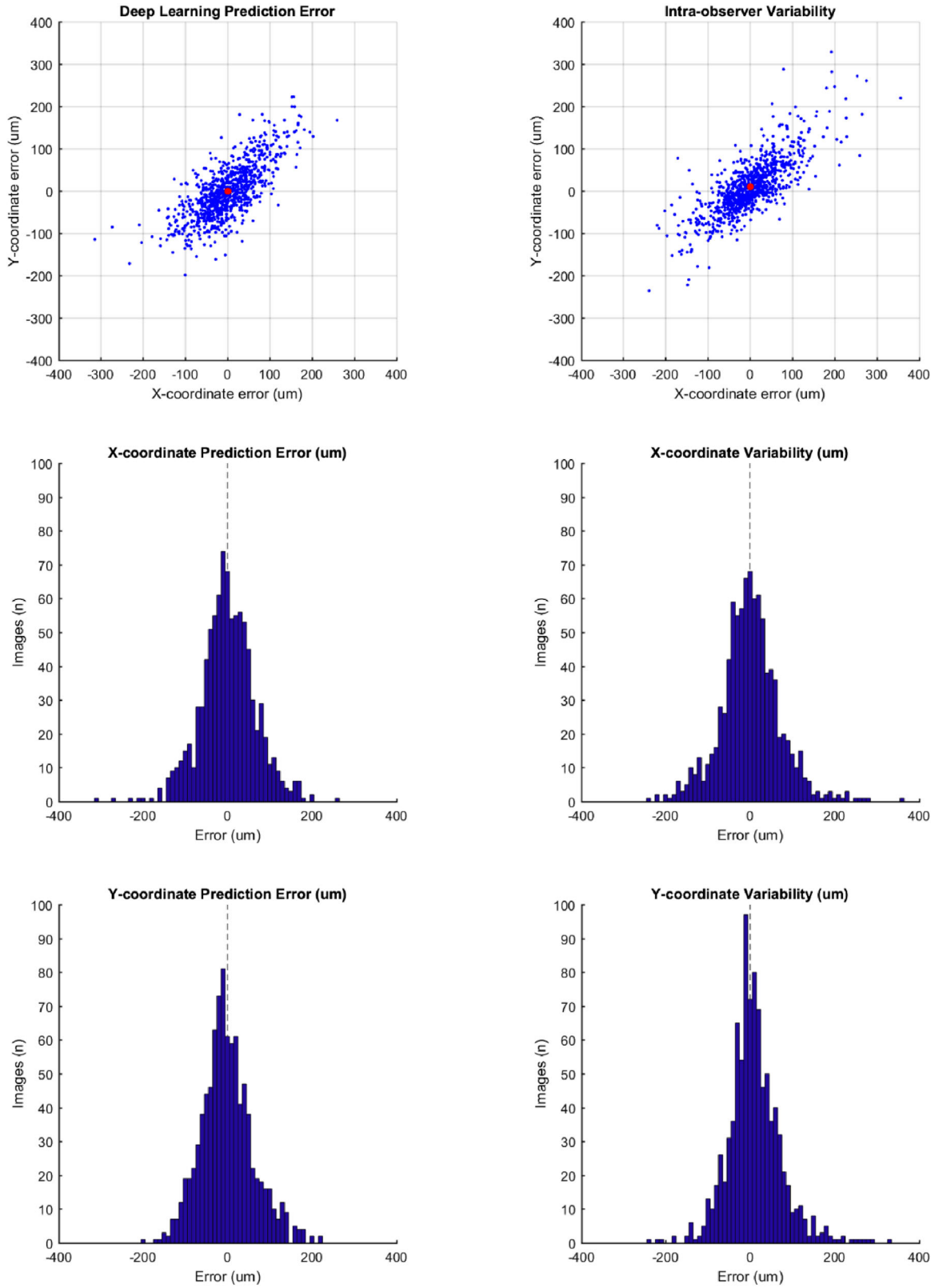
Figure 2. Distribution of CNN-predicted and intraobserver errors in scleral spur location definition. (Top) Scatter plots of CNN-predicted errors (left) and intragrader errors (right). Mean error plotted in red. (Middle) Histograms of X-coordinate CNN prediction (left) and intraobserver (right) errors. (Bottom) Histograms of Y-coordinate CNN prediction (left) and intraobserver (right) errors.
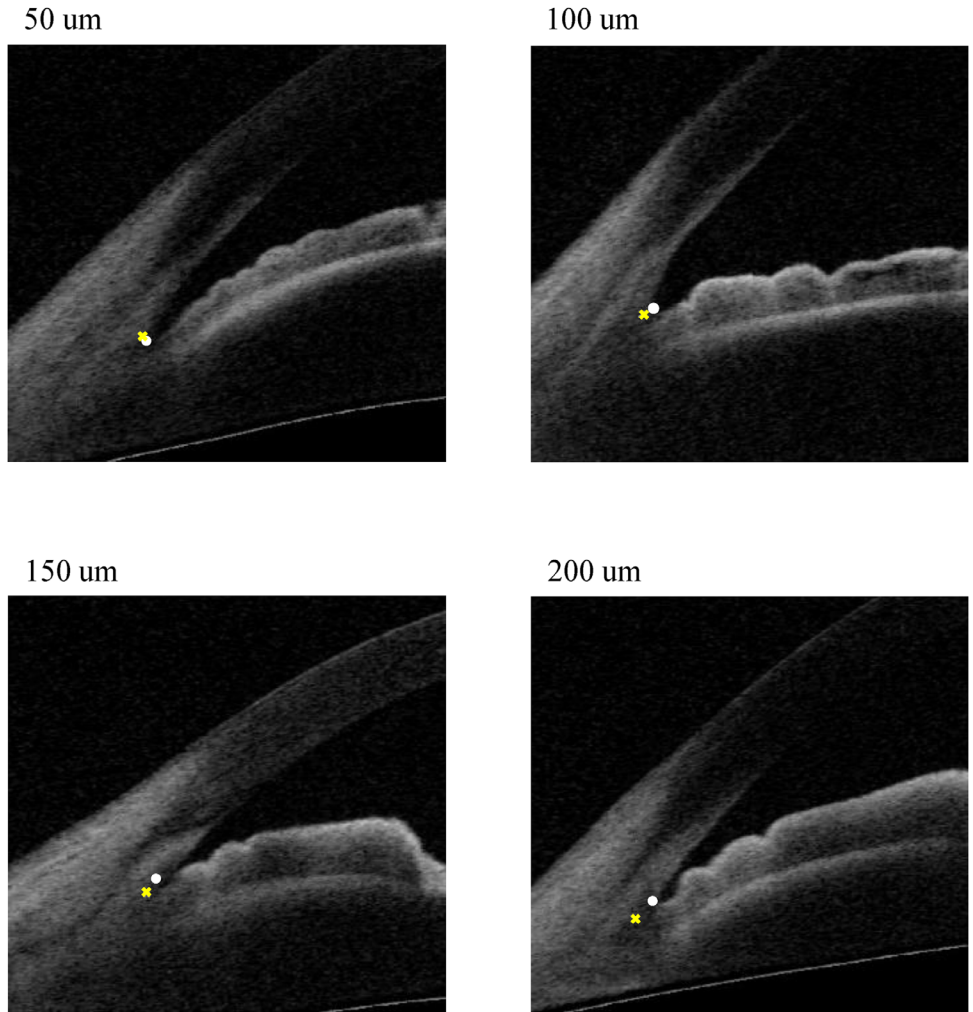
50 um

100 um

150 um

200 um

Figure 3.   Representative images of various absolute distances (50, 100, 150, and 200 μm) between reference grader-marked (cross) and CNN-predicted (circle) scleral spur locations.
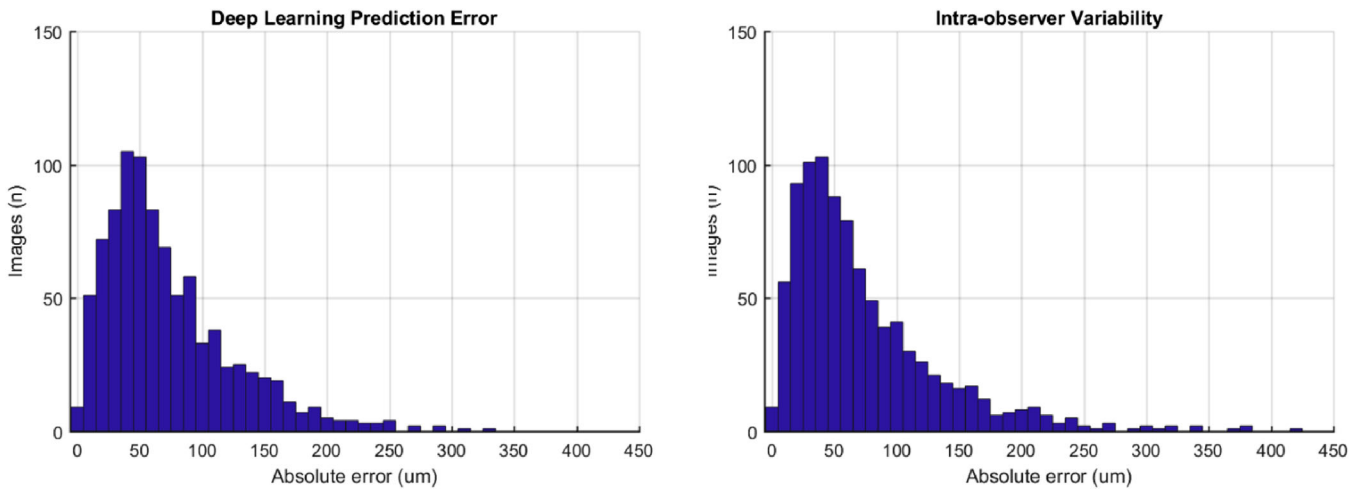

Figure 4.   Histograms of absolute CNN-predicted (left) and intraobserver (right) errors in scleral spur location.

reference – CNN, reference – grader 1 (new), and reference – grader 2. The Wilcoxon signed-ranked test revealed that the distributions of errors for reference – CNN and reference – grader 1 were similar for both X-coordinates ($P = 0.609$) and Y-coordinates ($P = 0.378$). The same test demonstrated that the distributions of errors for reference – grader 1 (new) and reference – grader 2 were dissimilar for both X- (signed-rank test; $P < 0.001$) and Y-coordinates (signed-rank test; $P < 0.001$).

The mean prediction error increased when the CNN was re-trained with smaller subsets of the training dataset (Supplementary Fig. S2). Mean prediction error declined to a stable absolute value of approximately 75 µm when the CNN model was developed using 30% or more of the training dataset.

Discussion

In this study, we developed and tested a deep neural network model that detects the scleral spur in AS-OCT images. The CNN was based on the ResNet-18 architecture and achieved human expert level performance; the distribution of prediction errors by the CNN model was similar to intragrader variability by the human grader who provided reference labels of scleral spur locations. These prediction errors were also significantly smaller than the intergrader variability observed between human expert graders. To our knowledge, this is the first fully automated method for detecting the scleral spur in AS-OCT images at a human expert level, even in eyes with angle closure. We believe this method resolves a long-standing limitation in the field of AS-OCT imaging and could greatly enhance the utility of AS-OCT imaging for clinical care and scientific research.

The scleral spur is the key anatomic landmark in the detection of ITC, which defines angle closure based on qualitative analysis of AS-OCT images. Previous studies demonstrated that ITC is sometimes missed on gonioscopy despite being more predictive of incident gonioscopic angle closure and primary angle closure disease (PACD).[15,29] Therefore, an automated method to detect the scleral spur and ITC would facilitate a more thorough evaluation of the ACA and earlier detection of patients at risk for angle closure disease. This method would be especially beneficial for clinicians who are inexperienced with manual interpretation of AS-OCT images. Deep learning methods were applied to develop a CNN model that detects a specific amount of ITC (more than one-third of the width of the TM) on AS-OCT images.[25] However, it is currently unclear what degree of ITC is clinically significant and affects the aqueous outflow function of the eye. There-

fore, direct detection of the scleral spur allows for more flexible assessments of the ACA for ITC.

Automated detection of the scleral spur also has important implications for developing and testing new quantitative methods to evaluate and monitor patients with primary angle closure disease. A recent landmark randomized controlled trial demonstrated that gonioscopy is poorly able to identify which patients with early primary angle closure disease are at higher risk of disease progression.[30] This finding may be related to the fact gonioscopy grades are only weakly associated with angle width in eyes with angle closure.[31] Conversely, quantitative AS-OCT measurements of angle width have a strong association with intraocular pressure, a strong risk factor for glaucomatous optic neuropathy, in a subset of eyes with primary angle closure disease.[32] However, the clinical utility of this finding is currently limited by the technical challenges associated with manual analysis of AS-OCT images. Automating quantitative analysis of AS-OCT images could also facilitate monitoring the progression of angle narrowing and closure over time. Trend-based analysis of angle width is not possible with gonioscopy, which has led to a lack of consensus on how often patients with early primary angle closure disease should be monitored or when they should be treated.

We assessed the performance of our CNN model by comparing it to the intragrader reproducibility of a human expert grader with more than 20,000 images of experience. There was no significant difference in the X- and Y-coordinate distributions of prediction errors for the CNN and intragrader variability for the human grader. In addition, absolute errors were similar for the CNN model and human grader, with 75% and 90% of absolute prediction errors fell within 100 µm and 150 µm of reference scleral spur locations, respectively. However, assessing the performance of the CNN model in absolute terms is more challenging. One previous study used 80 µm along both the X- and Y-axes as a cutoff for clinically significant variability in detecting scleral spur location.[14] That study reported intragrader reproducibility of 84% within 80 µm, which is similar to the 81% by the CNN model and 80% by the reference grader in our study. That study also reported intergrader reproducibility of 77% within 80 µm, compared with 73% in our study. However, these results should be interpreted with some caution because that study was based on 31 multiethnic eyes, whereas our study was based on 2333 eyes of a single ethnicity, which likely contributed to differences in image quality and distributions of scleral spur locations.

The scleral spur can be more difficult to detect in eyes with angle closure owing to attenuation of the OCT signal in portions of the ACA with ITC. We

assessed the performance of our CNN model in subsets of images from open angle and angle closure eyes to determine if angle status had any effect on the accuracy of predicted scleral spur coordinates. Overall, mean prediction errors and intragrader and intergrader variability were greater in eyes with angle closure. However, this difference was actually smaller for prediction errors by the CNN model compared with intragrader variability by the reference grader. This finding suggests that the CNN model can capably detect the scleral spur, even in angle closure eyes.

Our methods have some limitations. Reference scleral spur labels were provided by one human grader with experience marking the scleral spur in more than 20,000 images. However, scleral spur detection is subjective, and it remains a possibility that scleral spur locations predicted the CNN model will not generalize to other graders. It is reassuring that intergrader variability between expert graders in our study, one of whom provided the reference labels for CNN training, was comparable with the variability reported in another study.[14] Nevertheless, it could be beneficial to retrain the CNN model based on reference labels provided by a panel of expert graders now that its ability to replicate the performance of a single grader has been demonstrated. Similarly, our model may not generalize to images acquired on other AS-OCT devices. The location and appearance of the ACA can vary based on the AS-OCT device, and some devices are able to resolve fine anatomic structures, such as the TM. Therefore, we determined that a much smaller training dataset composed of approximately 8000 images could be enough to obtain comparable performance should the CNN model need to be retrained using a different dataset. Finally, although our CNN model is highly effective at detecting the scleral spur, it is unclear how mislocalizing the scleral spur affects corresponding AS-OCT measurements. Therefore, future work should assess the biometric measurements associated with predicted scleral spur locations to rule out the possibility that small differences in scleral spur locations lead to significant differences in biometric measurements.

In summary, we used AS-OCT data from a population-based study of Chinese Americans to develop a deep neural network capable of detecting the scleral spur at the level of a human expert. This solves a major limitation faced by clinicians and researchers who use AS-OCT to manage or study patients with angle closure. We hope that this method will facilitate qualitative evaluation of the ACA for angle closure and development of quantitative clinical methods to manage patients at risk for primary angle closure glaucoma.

References

1. Tham YC, Li X, Wong TY, Quigley HA, Aung T, Cheng CY. Global prevalence of glaucoma and projections of glaucoma burden through 2040: a systematic review and meta-analysis. *Ophthalmology*. 2014;121:2081–2090.
2. Weinreb RN, Aung T, Medeiros FA. The pathophysiology and treatment of glaucoma: a review. *JAMA*. 2014;311:1901–1911.
3. He M, Friedman DS, Ge J, et al. Laser peripheral iridotomy in primary angle-closure suspects: biometric and gonioscopic outcomes. The Liwan Eye Study. *Ophthalmology*. 2007;114(3):494–500.
4. Azuara-Blanco A, Burr J, Ramsay C, et al. Effectiveness of early lens extraction for the treatment of primary angle-closure glaucoma (EAGLE): a randomised controlled trial. *Lancet*. 2016;388:1389–1397.
5. Radhakrishnan S, Chen PP, Junk AK, Nouri-Mahdavi K, Chen TC. Laser peripheral iridotomy in primary angle closure. *Ophthalmology*. 2018;125(7):1110–1120.
6. Rigi M, Bell NP, Lee DA, et al. Agreement between gonioscopic examination and swept source Fourier domain anterior segment optical coherence tomography imaging. *J Ophthalmol*. 2016;2016:1–8.
7. Izatt JA, Hee MR, Swanson EA, et al. Micrometer-scale resolution imaging of the anterior eye in vivo with optical coherence tomography. *Arch Ophthalmol*. 1994;112:1584–1589.
8. Ang M, Baskaran M, Werkmeister RM, et al. Anterior segment optical coherence tomography. *Prog Retin Eye Res*. 2018;66:132–156.

9. Shan J, DeBoer C, Xu BY. Anterior segment optical coherence tomography: applications for clinical care and scientific research. *Asia Pac J Ophthalmol*. April 2019 [Epub ahead of print].

10. Nongpiur ME, He M, Amerasinghe N, et al. Lens vault, thickness, and position in Chinese subjects with angle closure. *Ophthalmology*. 2011;118:474–479.

11. Ozaki M, Nongpiur ME, Aung T, He M, Mizoguchi T. Increased lens vault as a risk factor for angle closure: confirmation in a Japanese population. *Graefes Arch Clin Exp Ophthalmol*. 2012;250:1863–1868.

12. Wang B, Sakata LM, Friedman DS, et al. Quantitative iris parameters and association with narrow angles. *Ophthalmology*. 2010;117:11–17.

13. Wang BS, Narayanaswamy A, Amerasinghe N, et al. Increased iris thickness and association with primary angle closure glaucoma. *Br J Ophthalmol*. 2011;95:46–50.

14. Cumba RJ, Radhakrishnan S, Bell NP, et al. Reproducibility of scleral spur identification and angle measurements using Fourier domain anterior segment optical coherence tomography. *J Ophthalmol*. 2012;2012:1–14.

15. Sakata LM, Lavanya R, Friedman DS, et al. Comparison of gonioscopy and anterior segment ocular coherence tomography in detecting angle closure in different quadrants of the anterior chamber angle. *Ophthalmology*. 2008;115:769–774.

16. McKee H, Ye C, Yu M, Liu S, Lam DSC, Leung CKS. Anterior chamber angle imaging with swept-source optical coherence tomography: detecting the scleral spur, Schwalbe's line, and Schlemm's canal. *J Glaucoma*. 2013;22:468–472.

17. Pan X, Marion K, Maram J, et al. Reproducibility of anterior segment angle metrics measurements derived from cirrus spectral domain optical coherence tomography. *J Glaucoma*. 2015;24:e47–e51.

18. Xu BY, Mai DD, Penteado RC, Saunders L, Weinreb RN. Reproducibility and agreement of anterior segment parameter measurements obtained using the CASIA2 and Spectralis OCT2 optical coherence tomography devices. *J Glaucoma*. 2017;26:974–979.

19. Console JW, Sakata LM, Aung T, Friedman DS, He M. Quantitative analysis of anterior segment optical coherence tomography images: the Zhongshan angle assessment program. *Br J Ophthalmol*. 2008;92:1612–1616.

20. Nongpiur ME, Haaland BA, Friedman DS, et al. Classification algorithms based on anterior segment optical coherence tomography measurements for detection of angle closure. *Ophthalmology*. 2013;120:48–54.

21. Nongpiur ME, Haaland BA, Perera SA, et al. Development of a score and probability estimate for detecting angle closure based on anterior segment optical coherence tomography. *Am J Ophthalmol*. 2014;157:32–38.e1.

22. Sakata LM, Lavanya R, Friedman DS, et al. Assessment of the scleral spur in anterior segment optical coherence tomography images. *Arch Ophthalmol*. 2008;126:181–185.

23. Gulshan V, Peng L, Coram M, et al. Development and validation of a deep learning algorithm for detection of diabetic retinopathy in retinal fundus photographs. *JAMA*. 2016;316:2402–2410.

24. Ting DSW, Cheung CYL, Lim G, et al. Development and validation of a deep learning system for diabetic retinopathy and related eye diseases using retinal images from multiethnic populations with diabetes. *JAMA*. 2017;318:2211–2223.

25. Fu H, Baskaran M, Xu Y, et al. A deep learning system for automated angle-closure detection in anterior segment optical coherence tomography images. *Am J Ophthalmol*. 2019;203:37–45.

26. Xu BY, Chiang M, Chaudhary S, Kulkarni S, Pardeshi AA, Varma R. Deep Learning Classifiers for Automated Detection of Gonioscopic Angle Closure Based on Anterior Segment OCT Images. *Am J Ophthalmol*. 2019;208:273–280.

27. Russakovsky O, Deng J, Su H, et al. ImageNet large scale visual recognition challenge. *Int J Comput Vis*. 2015;115:211–252.

28. Pan SJ, Yang Q. A survey on transfer learning. *IEEE Trans Knowl Data Eng*. 2010;22:1345–1359.

29. Baskaran M, Iyer JV, Narayanaswamy AK, et al. Anterior segment imaging predicts incident gonioscopic angle closure. *Ophthalmology*. 2015;122:2380–2384.

30. He M, Jiang Y, Huang S, et al. Laser peripheral iridotomy for the prevention of angle closure: a single-centre, randomised controlled trial. *Lancet* 2019;393:1609–1618.

31. Xu BY, Pardeshi AA, Burkemper B, et al. Quantitative evaluation of gonioscopic and EyeCam assessments of angle dimensions using anterior segment optical coherence tomography. *Transl Vis Sci Technol*. 2018;7:33.

32. Xu BY, Burkemper B, Lewinger JP, Jiang X, et al. Correlation between Intraocular Pressure and Angle Configuration Measured by OCT. *Ophthalmol Glaucoma*. 2018;1:158–166.